In situ synthesis of PuCl3 and corresponding Raman and density functional theory vibrational modes

Hanson, Alexa Brooke
Hubley, Nicholas Thomas
Atta-Fynn, Raymond
Batista, Enrique Ricardo
Hernandez, Sarah Christine
Scott, Brian Lindley

To be published in: Journal of Raman Spectroscopy

DOI to publisher's version: 10.1002/jrs.6597

Hanson Alexa (Orcid ID: 0000-0001-8521-1189)

In-situ Synthesis of $PuCl_3$ and Corresponding Raman and Density Functional Theory Vibrational Modes

Alexa Hanson[a], Nicholas Hubley[b], Raymond Atta-Fynn[c], Enrique Batista[d], Sarah Hernandez[c], Brian Scott[a]

[a]Material Synthesis and Integrated Devices Division, [b]Actinide Analytical Chemistry Division, [c]Nuclear Materials Science Division, [d]Center for Nonlinear Studies. Los Alamos National Laboratory, Los Alamos, NM 87545, USA

Abstract

The experimental and calculated Raman spectrum of $PuCl_3$ has been reported for the first time. $PuCl_3$ is a primary species found in plutonium metal refinement, specifically in pyrochemical salt processes including multicycle direct oxide reduction, metal chlorination, and electrorefining. As such, Raman signatures of $PuCl_3$ could serve as potential forensic indicators of material process history. A novel technique for synthesizing $PuCl_3$ from the in-situ chlorination of plutonium metal with HCl was developed to establish these signatures. Cerium metal surrogates were utilized to ensure optimization of the plutonium experiments and to minimize personnel exposure, and all experiments were carried out in a Raman reaction chamber designed for air-tight, high vacuum environments. In-situ Raman spectroscopy was employed in conjunction with Density Functional Theory (DFT) to investigate the vibrational modes of $PuCl_3$. Associated mixed oxy and hydroxyl phases are also reported. The combined Raman and DFT results have eliminated inconsistencies in Raman mode assignments for the MX_3 family of metal chlorides having $P6_3/m$ symmetry, and IR modes derived from the DFT calculations are additionally presented. The data observed in this study is of potential interest to nuclear forensic analyses, nuclear sample aging, nuclear energy, plutonium processing, and stockpile stewardship.

1. Introduction

Traditionally, plutonium is produced in nuclear reactors from burn up of uranium oxide fuel, separated using the PUREX process, and converted to PuO_2 for reduction to high purity plutonium metal for use in nuclear weapons. Plutonium metal production utilizes recycled and scrap material that require refinement by a variety of technologies known as pyrochemical salt processing.[1] The purification of plutonium metal generates an assortment of byproducts, and the physical and chemical signatures of these byproducts can serve as potential use to nuclear forensic analyses, prediction of nuclear material aging, nuclear energy applications including thermoelectric power production for deep space missions, improvement of production flowsheets through real time monitoring, and stockpile stewardship. This work therefore aims to elucidate signatures of a principal byproduct system in plutonium metal production, the plutonium-chloride system. Chlorides are utilized in pyrochemical salt processing methods to purify plutonium metal due to their low corrosion of containment materials,[2] and a primary species of interest found in multiple phases of plutonium metal refinement is $PuCl_3$.

The first phase in pyrochemical salt processing of plutonium is multicycle direct oxide reduction (MCDOR), in which PuO_2 purified by nitric and hydrochloric acid processing is converted to plutonium metal. The reaction occurs with calcium metal in a molten calcium chloride solvent and, following completion of the reaction, allows the resulting plutonium metal to meld at

This is the author manuscript accepted for publication and has undergone full peer review but has not been through the copyediting, typesetting, pagination and proofreading process, which may lead to differences between this version and the Version of Record. Please cite this article as doi: 10.1002/jrs.6597

the bottom of the reaction crucible while the calcium chloride forms a salt cake that solidifies atop the metal. The plutonium metal resulting from MCDOR is impure, and readily absorbs impurities from the $CaCl_2$ salt cake.[3] $PuCl_3$ could be present at this stage of metal refinement due to the absorption of chloride.

The subsequent process used for further purification is dependent upon the type of impurities present and corresponding material aging. As ^{241}Pu undergoes radioactive decay to form ^{241}Am, significant amounts of americium impurity must be removed via metal chlorination, formerly referred to as molten salt extraction or slagging,[1, 3] if the plutonium has been stored for an extended period of time. Metal chlorination involves melting the plutonium metal to be reacted with chlorine gas. This directly produces $PuCl_3$, which subsequently reacts to additionally form $AmCl_3$, and will then produce a removable salt cake on top of the metal after cooling.[4] The plutonium metal then undergoes the electrorefining process, which refines the metal to a purity acceptable for use in nuclear weapons. Electrorefining can also be completed in lieu of metal chlorination directly following MCDOR if the initial daughter product impurities are minimal.[3] In this process, the impure plutonium metal is melted and oxidized to $PuCl_3$ at the anode, which acts as a Pu(III) seeding agent to guarantee reduction at the cathode. The $PuCl_3$ is subsequently dissolved in the molten salt, and the molten plutonium is then transported to the cathode and reduced to pure plutonium metal for eventual use in nuclear weapons.[5-7] Ultimately, the bulk of impurities resulting from traditional plutonium pyrochemical salt processing are chloride salts, namely $PuCl_3$. This work therefore offers an investigation into the Pu-Cl system by synthesizing $PuCl_3$ via in-situ chlorination of plutonium metal to produce milligram amounts of material. In this fashion, signatures of small particles and metal surfaces, which are often the primary form of interdicted material, may be developed.

Commonly reported lanthanide and actinide chlorination pathways for trichloride formation are often conducted under high temperature environments and include the use of hydrochloric acid or chlorine gas as the chlorinating agent, where oxides, sesquioxides, and hydrides have been utilized as reactants.[8-15] Additionally, chlorination via molten salt mixtures, including LiCl-KCl, NaCl-$CaCl_2$, and metallic U has been widely reported, and include chlorinating agents such as $BiCl_3$,[16] $CdCl_2$,[17] $CuCl_2$,[18] $FeCl_x$,[19] NH_4Cl,[20] and $ZnCl_2$.[21, 22] UCl_3 synthesis can additionally be accomplished via hydrogen reduction of the tetrachloride.[23] Previously reported production pathways specific to $PuCl_3$ include direct chlorination of plutonium metal via elemental chlorine,[24] and chlorination of plutonium oxide or oxalate via chlorinating agents such as hexachloropropene,[25] PCl_5 and SCl_2,[24] and $COCl_2$ and CCl_4.[26] Additionally, chlorination via HCl at elevated temperatures has been reported for plutonium oxide, oxalate, and oxalate hydrate.[27-30]

In this study, a novel method for synthesizing and characterizing $PuCl_3$ in-situ has been developed in which plutonium metal is chlorinated via HCl at ambient temperature. This method is advantageous in that it employs small amounts of plutonium (~10 mg), does not require the use of chlorine gas or a high temperature environment, and in-situ synthesis and analysis of $PuCl_3$ lowers the risk of radioactive contamination. Furthermore, eliminating the use of molten salts omits the chance of minor component contamination. The reaction occurs by the following equation:

$$2Pu^0(s) + 6HCl(aq) \rightarrow 2PuCl_3(s) + 3H_2 \quad (1)$$

To ensure success of the plutonium experiments and to minimize personnel exposure, several optimizing iterations of surrogate experiments were carried out with polished cerium metal,

which is a well-known proxy of plutonium due to its similarities in crystal and electronic structures and will therefore produce similar and predictable Raman shifts.[31] Success of the $CeCl_3$ experiments was confirmed via spectral comparison of commercially available $CeCl_3$. Density functional theory (DFT) was additionally utilized to offer further interpretation of the experimental work, and to aid in the assignment of Raman bands.

While $PuCl_3$ and tangential phases have been previously characterized by powder X-ray diffraction (p-XRD), local defects caused by intrinsic decay or aging environments cannot be directly measured by this technique. As such, Raman spectroscopy has recently been utilized to establish signatures of local defect modes in materials such as PuO_2 with short term alpha decay damage and determining sample age since calcination,[32] long term alpha decay damage,[33] and laser induced annealing.[34] Moreover, Raman spectroscopy can be utilized to characterize residual amounts of material on a surface, whereas XRD cannot, and is more amenable to the use of handheld instruments for in field investigations. Further development of these signatures will ultimately provide insight to the provenance of plutonium materials in interest to nuclear forensics, and thus, the goal of this study is to develop Raman signatures of $PuCl_3$ and represents the first time the Raman and DFT calculated spectra of $PuCl_3$ have been reported.

2. Experimental

2.1. Materials

Caution! These plutonium materials are high specific-activity α-particle emitters, along with associated γ-ray emissions, in addition to β-particle emission from daughters. These radiological hazards (and heavy metal chemical toxicity) pose serious health threats. Hence, all studies were conducted with appropriate controls for the safe handling and manipulation of radioactive materials, i.e., in a United States Department of Energy-regulated radiological laboratory equipped with HEPA filtered hoods and continuous air monitors. All free-flowing solids that contained transuranium elements were handled in negative-pressure gloveboxes.

A plutonium metal coupon (2 wt% Ga alloy) containing a mixture of delta and alpha phase was obtained from Los Alamos National Laboratory (LANL) stock materials and possessed an oxide layer. XRD was used to confirm the phase purity of the plutonium coupon, and Raman spectroscopy was utilized to further verify whether the coupon had formed an outer oxidized layer of PuO_2. 8 M nitric acid, HNO_3, and a medium grained diamond file were used to remove the oxide layer. 12 M HCl was used as the direct chlorinating agent to produce $PuCl_3$ for subsequent measurement of Raman signatures.[35] Cerium metal was acquired from LANL stock materials. Furthermore, 99.9% ultra-dry $CeCl_3$ purchased from Thermo Fisher Scientific was utilized as reference material to confirm the success of the $CeCl_3$ experiments via Raman spectroscopy.

All experiments were carried out in-situ in a Raman reaction chamber purchased from Harrick Scientific (model number HVC-MRA-5) designed for air-tight, high temperature and high vacuum environments up to 910 ºC and 10^{-6} torr. The chamber was equipped with a vacuum line attached to a HEPA filtered turbopump backed by a rotary vane pump and a quartz window for sample viewing and Raman analysis.

2.2. Chlorination procedure for the plutonium coupon

Using a glove bag located in a fume hood, the plutonium coupon was transferred to a scintillation vial containing 8M HNO_3. The coupon was observed to react immediately on contact with the acid. The vial was sealed, cleaned, and transferred to a hot plate where it was heated

between 60-100ºC for 45 minutes to dissolve the oxide layer. While the most common PuO_2 dissolution procedure reported in literature involves HNO_3-HF solutions, particularly with the dissolution of high-fired oxides,[36] the present study has found 8 M HNO_3 to be a sufficient dissolution medium for the oxide layer grown under ambient conditions.

Following heating, the coupon was removed from the acid solution and washed with acetone before being transferred back into the glove bag. The coupon was further polished via diamond file which easily removed any remaining visible oxide layer and was then adhered to a piece of carbon tape on the sample stage in the reaction chamber. A drop of 12 M HCl was wicked onto the metal which reacted vigorously for 10 to 15 seconds. The reaction chamber was then sealed and evacuated to a pressure of $3.5 \cdot 10^{-6}$ torr to prevent material hydration and oxidation. A HEPA filter was installed between the reaction chamber and the vacuum pump, and the pump exhaust was vented back into the HEPA filtered fume hood as an extra precaution to prevent contamination.

2.3. X-ray diffraction

p-XRD was used to confirm the phase purity of the plutonium coupon prior to chlorination (Supporting Information Fig. S1), as well as the experimental $CeCl_3$ (Fig. S2). The $CeCl_3$ scan was collected on a Bruker AXS D8 Advance diffractometer equipped with an unconditioned Cu source and 1-D Si(Li) Lynxeye detector with a Ni filter. The sample was spun at a rate of 15 rpm. The resulting spectrum was analyzed via JADE XRD pattern processing software.[37]

2.4. Raman spectroscopy

The experimental $CeCl_3$, $CeCl_3$ reference material, experimental $PuCl_3$, and the unreacted plutonium metal coupon were analyzed utilizing a ThermoFisher Scientific DXRxi Raman imaging microscope. All scans were collected using a 532 nm excitation wavelength, 10x objective, and 1000 scans, and analyzed via OMNICxi and Origin software.[38, 39] The system was equipped with a DXR 532 nm full range grating of 900 lines/mm. The Pu sample data was collected using a 25 µm confocal pinhole or 50 µm slit and, depending on which spectrograph aperture was employed, exposure times between 0.33 and 1.0 s and power levels from 0.20 to 2.0 mW.

Experimental $CeCl_3$ data was measured using a 25 µm slit, 0.5 s exposure times, and 5 mW power level. $CeCl_3$ reference material data was collected using a 50 µm slit, an exposure time of 0.33 s, and power levels from 3.0 to 10 mW.

2.5. Density functional theory (DFT)

To offer interpretation of the experimental work, DFT was utilized to calculate the $PuCl_3$ Raman spectrum. DFT[40, 41] calculations were carried out on the $PuCl_3$ crystal using the Quantum Espresso code.[42] The Perdew-Burke-Ernzerhof (PBE) formulation to the generalized gradient approximation (GGA) to the DFT exchange-correlation functional was employed.[43] Norm-conserving Troullier-Martins pseudopotentials [44] modified into the Kleinman-Bylander separable form were used to describe the ion-electron interactions.[45] The Kohn-Sham orbitals and electron charge density were expanded using plane waves basis with energy cut-offs of 170 Ry and 680 Ry, respectively. A 6×6×11 Monkhorst-Pack [46] k-point grid with the first-order Methfessel-Paxton electronic smearing function [47] of width 0.005 Ry was employed for the Brillouin zone integration.

Fig. 1 depicts the primitive unit cell of $PuCl_3$ containing two Pu atoms and six Cl atoms. It has been previously determined that $PuCl_3$ possesses a hexagonal lattice structure and a $P6_3/m$ space group with lattice constants $a=b=7.394$ Å and $c=4.243$ Å. The Pu and Cl atoms are located

at Wyckoff positions of (1/3, 2/3, 1/4) and (x_0, y_0, 1/4), respectively, where x_0 = 0.3879 and y_0 = 0.3021 are internal crystal coordinates.[48] Thus, the lattice constants a, b, c that determine the crystal volume, and the internal parameters x_0 and y_0 must be optimized using DFT to obtain the ground state crystal structure.

The atomic positions and cell volume of bulk $PuCl_3$ were simultaneously optimized subject to the following relaxation criteria: the total energy was accurate to 10^{-10} Ry, the magnitude of the atomic force on each atom was less than 1.5×10^{-6} Ry/Bohr, and the magnitude of each component of the stress tensor was less than 10^{-3} kbar. The optimized lattice constants were a=b=7.374 Å and c=4.150 Å, and the optimized internal parameters were x_0 = 0.3882 and y_0 =0.3071. Using the fully optimized structure, the 24 phonon eigenmodes and eigenvectors and the associated Raman spectra in the 8-atom $PuCl_3$ unit cell were computed within the Density Functional Perturbation Theory (DFPT) formalism.[49, 50]

3. Results and Discussion

3.1 Experimental $CeCl_3$ p-XRD Data

The experimental $CeCl_3$ p-XRD data is shown in Fig. S2. The sample is likely comprised of a mixture of cerium hydrate phases, primarily $CeCl_3(H_2O)_7$, with pure $CeCl_3$ and CeO_2 as minor component phases. The presence of water and oxygen impurities is representative of real world samples which may have been exposed to various environmental conditions such as relative humidity. While p-XRD was not collected for the $PuCl_3$ sample due to the difficulty of sample handling, it is reasonable to assume the sample consisted of similar crystalline hydrate and oxide phases, which is discussed further in the following sections alongside associated Raman bands.

3.2. Experimental and Reference $CeCl_3$ Raman Data

The space group $P6_3/m$ corresponds to a unit cell symmetry of C_{6h}^2,[51] which is isomorphic with the underlying C_{6h} point group.[15] The phonons at the Γ point, i.e. Brillouin zone center, determine the Raman-active and infrared modes. The C_{6h} point group comprises 8 real irreducible symmetry representations: A_g, B_g, A_u, B_u, E_{1g}, E_{2g}, E_{1u}, and E_{2u}. Thus, the irreducible representation of the 24 phonon eigenmodes in $PuCl_3$ at the Γ point is:

$$\Gamma_{C_{6h}} = 2A_g + 2B_g + 2A_u + 2B_u + 2E_{1g} + 6E_{2g} + 6E_{1u} + 2E_{2u} \quad (2)$$

Furthermore, the C_{6h} point group includes two ions per crystallographic unit cell and two atoms per Bravais unit cell, which implies six active Raman modes: three E_{2g}, two A_g, and one E_{1g}; the E_{2g} modes are expected to relate to translational movements of the complete rare earth Cl_3 groups, the A_g modes encompass movements of Cl^- ions in the xy plane, and the E_{1g} mode involves movement of these ions along the z-axis.[52]

The Raman data of the experimental $CeCl_3$ sample and $CeCl_3$ reference material is illustrated in Fig. 2. The peak intensities were normalized for comparative purposes as the spectra were collected under varying instrumental settings for optimal peak resolution. Both the synthesized and reference $CeCl_3$ samples displayed largely equal Raman-active band locale, implying high success of the Ce surrogate experiments. Specifically, the experimental $CeCl_3$ samples exhibited three active bands at 104, 187, and 217 cm^{-1}. This agrees with previous work conducted at room temperature.[10] The absence of one of these modes, the middle lying E_{2g}, can likely be explained by a superposition of the middle lying missing E_{2g} mode and the A_g mode

occurring near 179 cm^{-1}.[53] The lowest lying A_g mode and the highest lying E_{2g} mode were additionally not resolved in this work. Notably, other studies have conducted Raman analysis for single crystal $CeCl_3$ and other isostructural lanthanide chlorides under high temperature conditions to increase peak resolution [15, 53, 54] and thus, it is likely that the absent modes were not identified in this work due to low scattering intensity.

The $CeCl_3$ reference material showed three active bands at 103, 184, and 212 cm^{-1}. The experimental $CeCl_3$ contains residual CeO_2 from the oxidized metal, with bands centered at 470 cm^{-1}.[55, 56] Additionally, minor structure around 300 cm^{-1} and 345 cm^{-1}, observable in Fig. 2b, may additionally be attributed to CeO_2 or Ce-Cl vibrations of a cerium hydroxyl chloride complex and Ce-O vibrations of the complex, respectively, which may occur due to hydroxylated and chlorinated CeO_2 material reacted with the concentrated HCl to produce mixed oxy and hydroxy chloride surface features on the oxide particles.[57, 58] Further structure from 3300 to 3500 cm^{-1} is attributed to O-H stretching due to the presence of water.[59] This is corroborated by the p-XRD data, which indicated the presence of $CeCl_3$ hydrate and oxide crystalline phases. The broad structure from 1100 to 1200 cm^{-1} is likely due to 2LO overtone,[60] while structure around 1600 cm^{-1} can likely be attributed to graphitic carbon, which suggests the presense of some residual organic material likely introduced from the oil the Ce metal was stored in.[61] The reference $CeCl_3$ spectrum additionally shows minor peaks at 65 cm^{-1} and 145 cm^{-1}. No published assignments could be identified for these peaks, however, similar structure has been observed in $LaCl_3$ and the UCl_3-type hexagonal form of $GdCl_3$.[10, 62]

3.3. Experimental and Calculated $PuCl_3$ Raman Data

Comparable to the $CeCl_3$ spectra, Raman-active bands were observable in the experimental $PuCl_3$ spectrum at 80, 181, 189, and 216 cm^{-1}. The middle and highest lying E_{2g} modes were similarly not resolved. The $PuCl_3$ spectrum also exhibited a broad band around 470 cm^{-1} representative of PuO_2. The presence of PuO_2 can be attributed to either residual oxide from the metal coupon or from material oxidation during the chlorination process prior to the sample chamber being evacuated. Structure from 685 cm^{-1} to 745 cm^{-1} is assigned to hydroxyl and water librational modes,[63] which would be expected from residual water in the cell from the 12 M HCl chlorinating agent. Oxyhydroxide and oxychloride phases may be present in real world samples from exposure of $PuCl_3$ to atmospheric oxygen and water.[64] Specifically, $Pu(OH)_2Cl$ can form as a result of water radiolysis, while $PuOCl_x$ can occur as an impurity in spent salts from pyrochemical salt processing.[65] Similarly to the experimental $CeCl_3$ sample, the minor structure around 1400 cm^{-1} and the peak at 1600 cm^{-1} are likely attributed to graphitic carbon, which suggests the presense of residual organic material,[61] which may have been present on the coupon from storage oil. The broad structure above this region and is likely attributed to material fluoresence.

The $PuCl_3$ bands at 181, 189, and 216 cm^{-1} exhibited a higher Raman shift compared to $CeCl_3$, while the band at 80 cm^{-1} exhibited a lower shift. This is due to the low wavenumber E_{2g} modes being the only modes with sizable contributions from the Pu and Ce atoms (see Fig. 4(a), discussed in detail below). Due to the large difference between the masses of Pu and Ce, Pu-induced vibrations will be smaller than that of Ce as vibrational frequency is inversely proportional to mass. Thus, the $PuCl_3$ E_{2g} mode at 80 cm^{-1} exhibits a lower shift compared to $CeCl_3$, and the remaining bands a higher shift.

The experimental and calculated $PuCl_3$ Raman spectra are presented in Fig. 3 with normalized peak intensity for comparative purposes. The calculated Raman spectrum was convoluted with a Gaussian function of width 2 cm^{-1}, and all six expected Raman-active modes

were identified at 89.8, 167.4, 180.9, 197.8, 214.0, and 222.6 cm^{-1}. The strongest peak corresponds to the A_g band at the 180.9 cm^{-1} wavenumber. The two peaks at 214 cm^{-1} and 222.6 cm^{-1}, corresponding to the A_g and the E_{2g} bands, respectively, are additionally of high intensity. The remaining two intensities correspond to the E_{2g} bands with wavenumbers of 89.8 cm^{-1} and 167.4 cm^{-1}.

The intensity of the calculated E_{1g} mode is extremely weak and not observable in Fig. 3. This may be due to the following reasons: the calculations did not incorporate spin-orbit coupling (SOC); correlation effects beyond DFT were not included for the Pu 5*f* electron states, i.e. DFT+U; the Raman tensor calculations for the PBE functional was only up to second order. The effects of SOC, DFT+U, and third order Raman tensor terms, which are necessary to fully capture the magnitude of the intensities, are not yet implemented in the Quantum Espresso code. Nevertheless, the remaining calculated wavenumbers are in sufficient agreement with the experimental intensities.

The calculated $PuCl_3$ wavenumbers are further illustrated in Table 1. Discarding the 3 lowest acoustic phonon frequencies in Equation 2, i.e. phonons of B_g, A_u, and E_{1u} symmetry, the remaining 21 frequencies are presented along with their corresponding group symmetry of the irreducible representation of the mode. The six Raman active modes are highlighted in red, and there are 10 total eigenmodes. Overall, the computed wavenumbers agree with the experimental data, despite the peak shifts discussed prior. However, the computed wavenumber for the A_g mode (mode 12; 180.9 cm^{-1}) is higher than the middle lying E_{2g} mode (modes 10,11; 167.4 cm^{-1}), while some previous lanthanide trichloride studies reported the A_g mode (162 cm^{-1}) to be lower than the E_{2g} mode (174 cm^{-1}).[53, 54] This discrepancy is likely due to electron correlation effects. Raman-active modes for a representative $CeCl_3$ sample, $CeCl_3$ reference material, experimentally synthesized $PuCl_3$, and $PuCl_3$ wavenumbers calculated by DFT are summarized in Table 2. The order of symmetry is reflective of the calculated $PuCl_3$ wavenumbers and previously reported work on $CeCl_3$ by Schaack and Koningstein.[52] Notably, additional previous studies have reported the middle lying E_{2g} mode to be of higher symmetry than the lowest lying *Ag* mode.[15, 53] It is reasonable to claim that the DFT calculations in this work have established the correct order of symmetry and thus addresses the inconsistencies in the literature for $CeCl_3$ mode assignments and MCl_3 species having $P6_3/m$ symmetry.

The $PuCl_3$ eigenvectors for the eigenmodes are schematically depicted in Fig. 4a-f. All modes, apart from modes 2 and 3, are dominated by Cl atomic vibrations, which is expected as Cl is much lighter than Pu. The modes consist mainly of twisting and rocking modes or a linear combination of both. For example, modes, 11, 12, 17 and 19 are twisting modes, modes 2 and 10 are rocking modes, and modes 16 and 20 are a linear combination of twisting modes.

These results establish the in-situ synthesis of $PuCl_3$ and the corresponding measurement and calculation of its Raman modes for the first time. Previously determined X-ray structures of the Pu and Ce analogs of the trichlorides are isostructural, sharing space group $P6_3/m$, suggesting they should have a similar number of vibrational bands, albeit with different energies based on differences in mass and bond stiffness from Ce to Pu. Our experimental Raman data agrees with this, showing four bands in similar energy regions for each system. The Raman measurements of $CeCl_3$, both synthesized and commercially sourced, agree with previously reported spectra. When compared to the $PuCl_3$ results reported in this work, the differences in Raman shifts are practical based on differences observed throughout the family of metal trihalide systems having the $P6_3/m$ structure type (*vide supra*). The agreement between the experimental and DFT calculated spectra are quite reasonable, and further establish the characterization of $PuCl_3$.

In future work, there are many other remaining plutonium processing signatures to understand in relation to plutonium halide signatures. Additional species relevant to plutonium forensic signatures include hydride species, which are bound by PuH_2 and PuH_3.[66] These species can occur in the presence of water such as relative humidity, or hydrogen, which can exist in storage containers due to water radiolysis.[67] Hydrogen environments can additionally exist due to radiolysis of hydrocarbon sources such as plastics used for bagging and storage.

Oxycarbides, PuO_xC_y, are also of particular interest and may suggest the presence of impurities in production as the pyrolysis of oxalate forms unbound carbon, which reacts with plutonium oxide to form oxycarbide phases. The oxalate ligand is used to precipitate Pu(III) or Pu(IV) from solution in the nitric acid purification process.[1] Carbon can also be introduced to the system by reduced surface phases interacting with CO and CO_2.[68] Finally, in addition to PuO_2, the sesquioxide, Pu_2O_3, is of interest as plutonium metal readily oxidizes in air to form a dual layered oxide system comprised of Pu_2O_3 at the metal interface and PuO_2 at the air-oxide interface.[69]

4. Conclusion

A novel method for the in-situ chlorination of plutonium metal with HCl to form $PuCl_3$ has been developed, and corresponding experimental and DFT calculated Raman spectra have been presented for the first time. Three Raman active bands for experimental $CeCl_3$ samples were observed at 104, 187, and 217 2 cm^{-1}, which are in agreement with previous $CeCl_3$ studies, as well as other isostructural lanthanide chlorides. Similarly, four active bands were observable in the experimental $PuCl_3$ spectrum at 80, 181, 189, and 216 cm^{-1}. Associated mixed oxy and hydroxyl phases were additionally presented, which are relevant to real world environmental conditions. The calculated $PuCl_3$ Raman spectrum includes six active bands at 89.8, 167.4, 180.9, 197.8, 214.0, and 222.6 cm^{-1}, and agree with the experimental results. The Raman signatures of $PuCl_3$ may be employed to establish the processing history of a plutonium sample to support nuclear forensic analyses and stockpile stewardship. Moreover, the DFT derived IR modes were presented and could also be employed to interpret IR spectra of future measurements of systems with potential $PuCl_3$ content. Finally, the combined Raman and DFT results have eliminated inconsistencies in Raman mode assignments for the MX_3 family of metal chlorides having $P6_3/m$ symmetry.

5. Acknowledgements

This work was supported by the US Department of Homeland Security's Office of Countering Weapons of Mass Destruction under Grant Number 70RWMD19K0000002. This document has been approved for unlimited release through Los Alamos National Laboratory under LA-UR-22-32514.

References

(1) Clark, D. L.; Jarvinen, G. D.; Migliori, A. *Actinide Research Quarterly, No. 3. Plutonium Processing at Los Alamos*; 2008.
(2) Mullins, L. J.; Leary, J. A.; Morgan, A. N.; Maraman, W. J. Plutonium Electrorefining. *Industrial and Engineering Chemistry Process Design and Development* **1962**, *2* (1), 20-24.
(3) Christensen, D. C.; Mullins, L. J. *Present Status of Plutonium Metal Production and Purification at Los Alamos—1982*; Los Alamos National Laboratory, 1983.
(4) Mullins, L. J.; Leary, J. A.; Maraman, W. J. Removal of Fission Product Elements by Slagging. *Industrial and Engineering Chemistry* **1960**, *52* (3), 227-230.
(5) Kolodney, M. Preparation of the First Electrolytic Plutonium and of Uranium from Fused Chlorides. In *Journal of The Electrochemical Society*, 1982; Vol. 129, pp 2438-2442.
(6) Kolodney, M. LA-148 Production of Plutonium by Electrolysis. 1944.
(7) Mullins, L. J.; Morgan, A. N. A Review of Operating Experience at the Los Alamos Plutonium Electrorefining Facility, 1963-1977. 1981.
(8) Okabe, P.; Newton, M.; Rappleye, D.; Simpson, M. F. Gas-solid reaction pathway for chlorination of rare earth and actinide metals using hydrogen and chlorine gas. *Journal of Nuclear Materials* **2020**, *534*.
(9) Salyulev, A. B.; Zakiryanova, I. D. Raman spectra of solid, molten, and gaseous gallium trichloride. *Russian Metallurgy (Metally)* **2010**, *2010* (2), 108-111.
(10) Daniel, J. F.; Wilmarth, W. R. Raman spectroscopic studies of gadolinium trichloride as a function of temperature. *Journal of Crystallographic and Spectroscopic Research* **1988**, *19* (1), 39-49.
(11) Spedding, F. H.; Porter, P. E.; Wright, J. M. Conductances of Aqueous Solutions of Some Rare Earth Chlorides at 25°. *Journal of the American Chemical Society* **1952**, *74* (8), 2055-2058.
(12) Bommer, H.; Hohmann, E. *On the Thermochemistry of the Rare Earths II: The Heats of Solution and of Formation of the Anhydrous Chlorides of the Rare Earths*; 1941.
(13) Anderson, A.; Mishra, B. Investigation of the Carbochlorination Process for Conversion of Cerium and Neodymium Oxides into Their Chlorides. *Journal of Sustainable Metallurgy* **2015**, *1*, 189-198.
(14) Zimmerman, J. B.; Ingles, J. C. Isolation of the Rare Earth Elements: A Chlorination-Volatilization Procedure. *Analytical Chemistry* **1960**, *32* (241-246).
(15) Asawa, C. K.; Satten, R. A.; Stafsudd, O. M. Depolarization of Raman Scattering in $LaCl_3$. *Physical Review* **1968**, *168* (3), 957-959.
(16) Bae, S.-E.; Cho, Y.-H.; Park, Y. J.; Ahn, H. J.; Song, K. Oxidation State Shift of Uranium during U(III) Synthesis with Cd(II) and Bi(III) in LiCl–KCl Melt. *Electrochemical and Solid-State Letters* **2010**, *13* (10), F25-F27.
(17) Li, S. X.; Vaden, D.; Westphal, B. R.; Frederickson, G. L.; Benedict, R. W.; Johnson, T. A. Integrated Efficiency Test for Pyrochemical Fuel Cycles. *Nuclear Technology* **2008**, *166* (2), 180-186.
(18) Westphal, B. R.; Price, J. C.; Mariani, R. D. Synthesis of Uranium Trichloride for the Pyrometallurgical Processing of Used Nuclear Fuel. In Fray International Symposium on Molten Salts and Ionic Liquids 2011, 2011.
(19) Zhang, H.; Newton, M. L.; Hamilton, D. E.; Simpson, M. F. High temperature UCl_3 synthesis in molten salt mixtures via reaction of U metal with iron chlorides. *Journal of Radioanalytical and Nuclear Chemistry* **2021**, *331*, 383-390.

(20) Eun, H. C.; Kim, T. J.; Jang, J. H.; Kim, G. Y.; Lee, S. J.; Hur, J. M. A study on chlorination of uranium metal using ammonium chloride. *Journal of Radioanalytical and Nuclear Chemistry* **2017**, *314* (1), 533-537.
(21) Kim, G.-Y.; Kim, T.-J.; Jang, J.; Eun, H.-C.; Lee, S.-J. Synthesis of uranium trichloride salt using ZnCl2. *Journal of Radioanalytical and Nuclear Chemistry* **2018**, *318*, 2173-2176.
(22) Lee, C. H.; Kim, T.-J.; Yoon, D.; Jang, J.; Kim, G.-Y.; Lee, S.-J. Efficient preparation of UCl3 by ZnCl2 mediated chlorination. *Journal of Radioanalytical and Nuclear Chemistry* **2019**, *322*, 331-336.
(23) Bradley, D. *The Preparation and Properties of the Chlorides of Uranium, Plutonium, Thorium, and of the Fission Product Chlorides*; United Kingdom Atomic Energy Authority Research Group, Atomic Energy Research Establishment, 1957.
(24) Abraham, B. M.; B., B. B.; Davidson, N. R.; F., H.; Karle, I.; Katz, J. J.; Wolf, M. J. Preparation and Properties of Plutonium Chlorides and Oxychlorides. *The Transuranium Elements* **1949**, 740-758.
(25) Christensen, E. L.; Mullins, L. J. *Preparation of Anhydrous Plutonium Trichloride*; USAEC Report LA-01431, Los Alamos National Laboratory, 1952.
(26) Tolley, W. B. *Plutonium Trichloride: Preparation by Reaction with Phosgene or Carbon Tetrachloride*; USAEC, AEC Research and Development, Metallurgy Unity, Applied Research Subsection, 1953.
(27) Reavis, J. G.; Johnson, K. W. R.; Leary, J. A.; Morgan, A. N.; Ogard, A. E.; Walsh, K. A. The Preparation of Plutonium Halides for Fused Salt Studies. In *Extractive and Physical Metallurgy of Plutonium and its Alloys, Symposium of the Metallurgical Society of AIME*, San Francisco, CA, 1959; Interscience Publishers, New York: pp 89-100.
(28) Cleveland, J. M. *Plutonium Handbook: A Guide to the Technology*; American Nuclear Society, 1980.
(29) Clark, D. L.; Hecker, S. S.; Jarvinen, G. D.; Neu, M. P. *The Chemistry of Actinide and Transactinide Elements*; Springer, 2008.
(30) West, M. H.; Ferran, M. D.; Fife, K. W. *The Chlorination of Plutonium Dioxide*; LA-11256, Los Alamos National Laboratory, 1988.
(31) Johansson, B. Crystal and electronic structure connections between the 4f and 5f transition metals. *Journal of Alloys and Compounds* **1995**, *223*, 211-215.
(32) Villa-Aleman, E.; Houk, A. L.; Shehee, T. C.; Bridges, N. J. Raman signatures from age-dating PuO_2 since last calcination. *Journal of Nuclear Materials* **2021**, *551*, 152969.
(33) Scott, B. L.; Pugmire, A. L.; Stritzinger, J. T.; Veirs, D. K.; Wolfsberg, L. E.; Wilkerson, M. P. Relationships between experimental signatures and processing history for a variety of PuO_2 materials. *Journal of Nuclear Materials* **2019**, *521*, 155-160.
(34) Villa-Aleman, E.; Dick, D. D.; Christian, J. H.; Foley, B. J. Laser-induced annealing of aged PuO2. *Journal of Raman Spectroscopy* **2021**, *52*, 1486-1489.
(35) Clark, D. L.; Geeson, D. A.; Hanrahan Jr., R. J. Plutonium Halides, Binary Plutonium Chlorides. In *Plutonium Handbook 2nd Edition*, 2019; p 1424.
(36) Kazanjian, A. R.; Stevens, J. R. Dissolution of plutonium oxide in nitric acid at high hydrofluoric acid concentrations. 1984; Vol. RFP-3609.
(37) Incorporated, M. D. JADE Pattern Processing, Identification, and Quantification Software Version 8.8. 2021.
(38) Scientific, T. F. OMNIC for Dispersive Raman 9.2.98.
(39) Corporation, O. OriginPro 2021b 9.8.5.201.

(40) Hohenberg, P.; Kohn, W. Inhomogeneous Electron Gas. *Physical Review* **1964**, *136* (3B), B864-B871.
(41) Kohn, W.; Sham, L. J. Self-Consistent Equations Including Exchange and Correlation Effects. *Physical Review* **1965**, *140* (4A), A1133-A1138.
(42) Giannozzi, P.; Baroni, S.; Bonini, N.; Calandra, M.; Car, R.; Cavazzoni, C.; Ceresoli, D.; Chiarotti, G. L.; Cococcioni, M.; Dabo, I.; et al. QUANTUM ESPRESSO: a modular and open-source software project for quantum simulations of materials. *Journal of Physics: Condensed Matter* **2009**, *21* (39), 395502.
(43) Perdew, J. P.; Burke, K.; Ernzerhof, M. Generalized Gradient Approximation Made Simple. *Physical Review Letters* **1996**, *77* (18), 3865-3868.
(44) Troullier, N.; Martins, J. L. Efficient pseudopotentials for plane-wave calculations. *Physical Review B* **1991**, *43* (3), 1993-2006.
(45) Kleinman, L.; Bylander, D. M. Efficacious Form for Model Pseudopotentials. *Physical Review Letters* **1982**, *48* (20), 1425-1428.
(46) Monkhorst, H. J.; Pack, J. D. Special points for Brillouin-zone integrations. *Physical Review B* **1976**, *13* (12), 5188-5192.
(47) Methfessel, M.; Paxton, A. T. High-precision sampling for Brillouin-zone integration in metals. *Physical Review B* **1989**, *40* (6), 3616-3621.
(48) Burns, J. H.; Peterson, J. R.; Stevenson, J. N. Crystallographic studies of some transuranic trihalides: $^{239}PuCl_3$, $^{244}CmBr_3$, $^{249}BkBr_3$ and $^{249}CfBr_3$. *Journal of Inorganic and Nuclear Chemistry* **1975**, *37* (3), 743-749.
(49) Gonze, X.; Lee, C. Dynamical matrices, Born effective charges, dielectric permittivity tensors, and interatomic force constants from density-functional perturbation theory. *Physical Review B* **1997**, *55* (16), 10355-10368.
(50) Baroni, S.; de Gironcoli, S.; Dal Corso, A.; Giannozzi, P. Phonons and related crystal properties from density-functional perturbation theory. *Reviews of Modern Physics* **2001**, *73* (2), 515-562.
(51) Fateley, W. G. Infrared and Raman Selection Rules for Lattice Vibrations: The Correlation Method. *Applied Spectroscopy* **1970**, *25* (2), 155-173.
(52) Schaack, G.; Koningstein, J. A. Phonon Frequencies of Rare Earth Trichlorides with Unit Cells of Different Dimensions. *Journal of Physics and Chemistry of Solids* **1970**, *31*, 2417-2420.
(53) Damen, T. C.; Kiel, A.; Porto, S. P. S.; Singh, S. The Raman Effects of $CeCl_3$ and $PrCl_3$. *Solid State Communications* **1968**, *6*, 671-673.
(54) Kiel, A.; Damen, T.; Porto, S. P. S.; Singh, S.; Varsanyi, F. Electronic Raman Effect in Paramagnetic Crystals: $CeCl_3$. *Physical Review* **1969**, *178* (3), 1518-1524.
(55) Schilling, C.; Hofmann, A.; Hess, C.; Ganduglia-Pirovano, M. V. Raman Spectra of Polycrystalline CeO_2: A Density Functional Theory Study. *The Journal of Physical Chemistry* **2017**, *121*, 20834-20849.
(56) Schweke, D.; Rubin, A.; Rabinovitch, L.; Kraynis, O.; Livneh, T. Cerium metal oxidation studied by IR reflection-absorption and Raman scattering spectroscopies. *Journal of Physics: Condensed Matter* **2022**, *34* (324002), 1-12.
(57) Zhang, L.; Cheng, Y.; Wang, X.; Hu, Q.; Zeng, Z.; He, D.; Lei, L. High-pressure Raman spectroscopy of CeOCl: Observation of the isostructural phase transition. *Journal of Raman Spectroscopy* **2019**, *50*, 1962-1968.

(58) Rudolph, W. W.; Irmer, G. Raman spectroscopic characterization of light rare earth ions: La^{3+}, Ce^{3+}, Pr^{3+}, Nd^{3+} and Sm^{3+} - hydration and ion pair formation. *Dalton Transactions* **2017**, *46*, 4235-4244.
(59) Tsvirko, M.; Svetashev, A. Raman spectroscopic study of trivalent lanthanides in concentrated aqueous solutions. *Journal of Physics: Conference Series* **2011**, *289*.
(60) Loridant, S. Raman spectroscopy as a powerful tool to characterize ceria-based catalysts. *Catalysis Today* **2021**, *373*, 98-111.
(61) Rosen, H.; Hansen, A. D. A.; Gundel, L.; Novakov, T. Identification of the optically absorbing component in urban aerosols. *Applied Optics* **1978**, *17* (24), 3859-3861.
(62) Sons, J. W. (2012-2021). Lanthanum Chloride Raman Spectrum. SpectraBase.
(63) Frost, R. L. Raman spectroscopy of selected copper minerals of significance in corrosion. *Spectrochim Acta* **2003**, *59*, 1195-1204.
(64) Weigel, F.; Wishnevsky, V.; Hauske, H. The vapor phase hydrolysis of $PuCl_3$ and $CmCl_3$: heats of formation of PuOCl and CmOCl. *Journal of The Less-Common Metals* **1977**, *56*, 113-123.
(65) Williamson, M. A.; Kleinschmidt, P. D. Thermodynamics and Sublimation Chemistry of Plutonium - Oxygen - Chlorine. In *15th Midwest High Temperature & Solid State Chemistry Conference*, Cornell University, Ithaca, NY, 1993.
(66) Haschke, J. M. *Evaluation of Source-Term Data for Plutonium Aerosolization*; Los Alamos National Laboratory, 1992.
(67) Haschke, J. M.; Allen, T. H. Plutonium hydride, sesquioxide and monoxide monohydride: pyrophoricity and catalysis of plutonium corrosion. *Journal of Alloys and Compounds* **2001**, *320*, 58-71.
(68) Larson, D. T.; Haschke, J. M. XPS-AES Characterization of Plutonium Oxdies and Oxide Carbide. The Existence of Plutonium Monoxide. In *Inorganic Chemistry*, 1981; Vol. 20.
(69) Butterfield, M. T.; Durakiewicz, T.; Guziewicz, E.; Joyce, J. J.; Arko, A. J.; Graham, K. S.; Moore, D. P.; Morales, L. A. Photoemission of surface oxides and hydrides of delta plutonium. *Surface Science* **2004**, *571*, 74-82.

Table 1. Phonon eigenfrequencies of $PuCl_3$ computed at the Γ point. Wavenumbers corresponding to Raman-active eigenmodes have been highlighted in red. The remaining eigenfrequencies represent IR-active eigenmodes.

Eigenmode label	Wavenumber (cm^{-1})	Symmetry
1	44.1	E_{1u}
2, 3	**89.8**	$\boldsymbol{E_{2g}}$
4	104.5	A_u
5	120.1	B_u
6, 7	134.6	E_{1u}
8, 9	162.6	E_{2u}
10,11	**167.4**	$\boldsymbol{E_{2g}}$
12	**180.9**	$\boldsymbol{A_g}$
13, 14	195.1	E_{1u}
15, 16	**197.8**	$\boldsymbol{E_{1g}}$
17	**214.0**	$\boldsymbol{A_g}$
18	215.9	B_g
19, 20	**222.6**	$\boldsymbol{E_{2g}}$
21	237.7	B_u

Table 2. Summary of resolved Raman-active modes in the experimental $CeCl_3$ samples, synthesized $PuCl_3$, and $PuCl_3$ modes calculated by DFT. Blank spaces indicate unresolved modes.

Mode	$CeCl_3$ (Experimental)	$CeCl_3$ (Reference)	$PuCl_3$ (Experimental)	$PuCl_3$ (DFT)
E_{2g}	104 cm^{-1}	103 cm^{-1}	80 cm^{-1}	89.8 cm^{-1}
E_{2g}			181 cm^{-1}	167.4 cm^{-1}
A_g				180.9 cm^{-1}
E_{1g}	187 cm^{-1}	184 cm^{-1}	189 cm^{-1}	197.8 cm^{-1}
A_g	217 cm^{-1}	212 cm^{-1}	216 cm^{-1}	214.0 cm^{-1}
E_{2g}				222.6 cm^{-1}

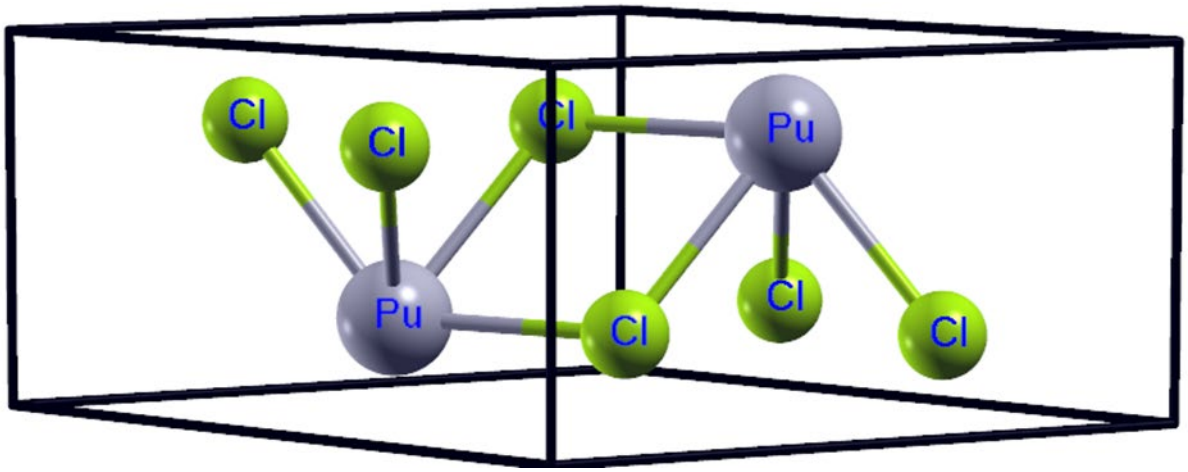

Figure 1. Depiction of the crystal structure of $PuCl_3$. The structure corresponds to the $P6_3/m$ space group (hexagonal lattice; space group number 176). The lattice constants are $a=b=7.394$ and $c=4.243$. The Wyckoff positions are Pu (1/3, 2/3, 1/4) and Cl (0.3879, 0.3021, 1/4).

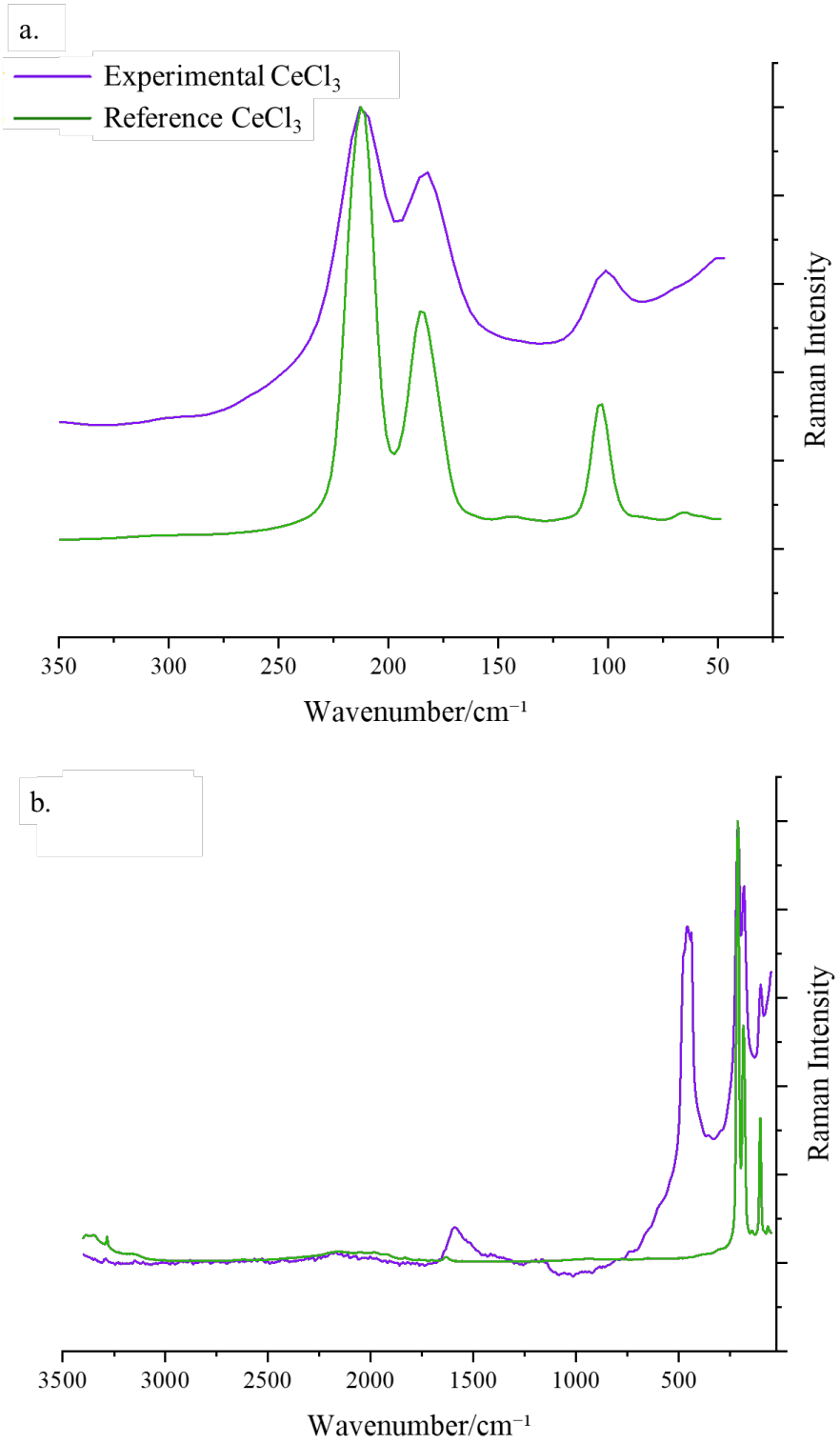

Figure 2. Normalized Raman spectra representative of synthesized surrogate $CeCl_3$ sample (purple) and commercial $CeCl_3$ reference material (green). (a) illustrates the resolved $CeCl_3$ modes while (b) shows the complete Raman spectrum where mixed oxy and hydroxyl modes were additionally observed.

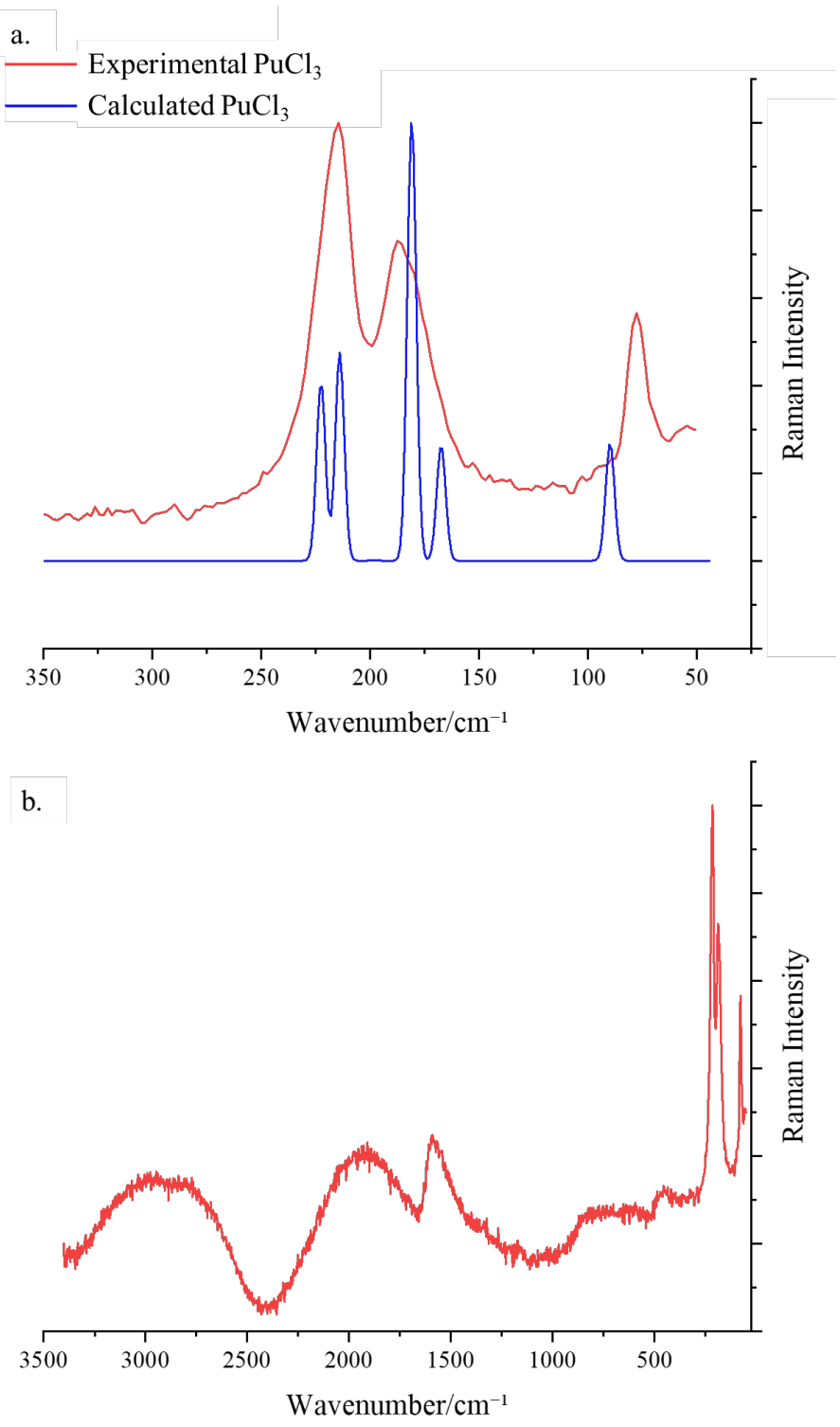

Figure 3. Normalized Raman spectra of synthesized $PuCl_3$ (red) and $PuCl_3$ calculated by DFT (blue). (a) illustrates the resolved $PuCl_3$ modes while (b) shows the complete Raman spectrum where, similarly to the $CeCl_3$, mixed oxy and hydroxyl modes were additionally observed.

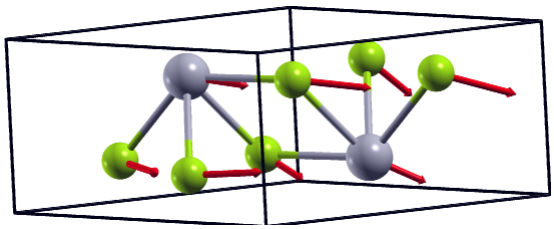

Figure 4a: E_{2g}, 89.8 cm^{-1}: Mode 2

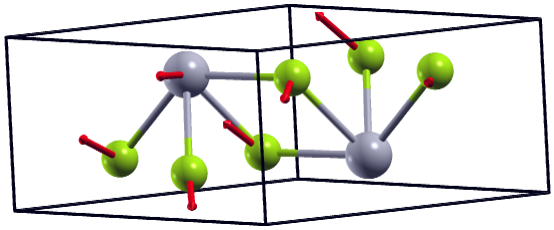

Mode 3

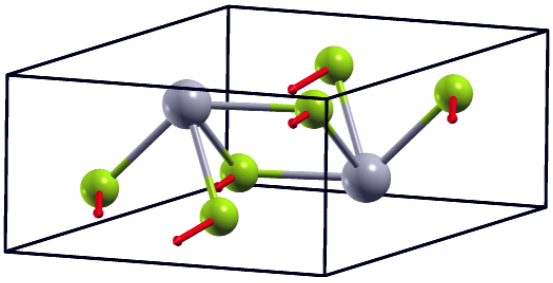

Figure 4b: E_{2g}, 167.4 cm^{-1}: Mode 10

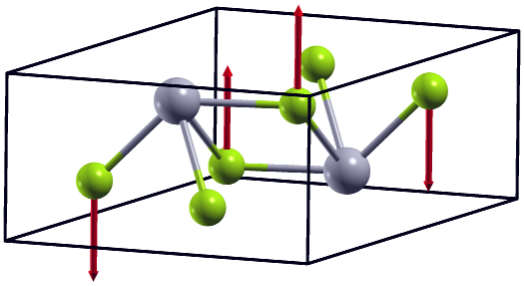

Mode 11

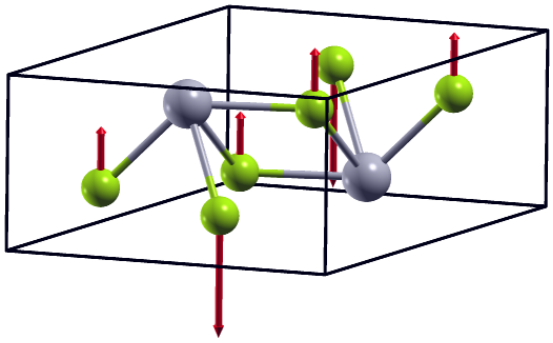

Figure 4c: A_g, 180.9 cm^{-1}: Mode 12

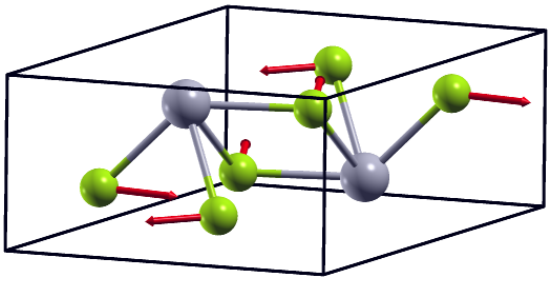

Figure 4d: E_{1g}, 197.8 cm^{-1}: Mode 15

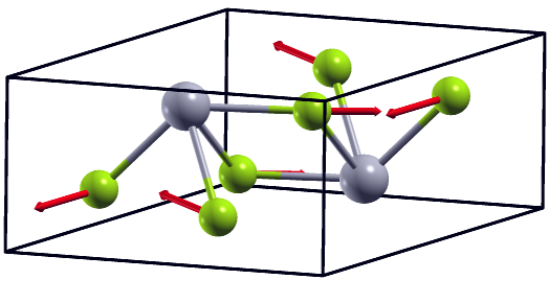

Mode 16

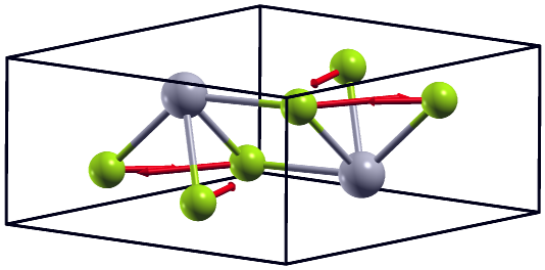

Figure 4e: A_g, 214 cm^{-1}: Mode 17

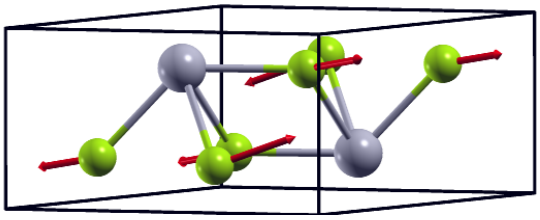

Figure 4f: E_{2g}, 222.6 cm^{-1}: Mode 19

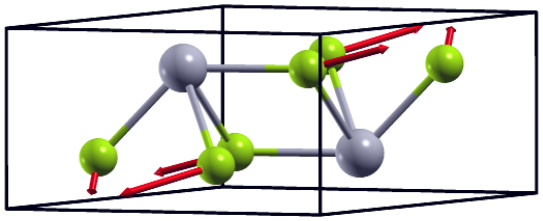

Mode 20

Figure 4. Calculated $PuCl_3$ eigenvectors for corresponding eigenmodes.